Bottom-up Structural Design of Crystalline Drug-Excipient Composite Microparticles via Microfluidic Droplet-based Processing

Eunice W. Q. Yeap,[†] Denise Z. L. Ng,[†] Ammu Prhashanna,[†] Ambika Somasundar,[†] Andrew J. Acevedo,[§] Qisong Xu,[‡] Fatma Salahioglu,[‡] Marc V. Garland,[‡] and Saif A. Khan*,[†]

[†]Department of Chemical and Biomolecular Engineering, National University of Singapore, 4 Engineering Drive 4, Singapore 117576, Singapore

[§]Department of Biomedical Engineering, Boston University, 44 Cummington Street, Boston, Massachusetts 02215, United States

[‡]Institute of Chemical and Engineering Sciences, A*STAR (Agency for Science, Technology and Research), 1 Pesek Road, Jurong Island, Singapore, 627833, Singapore

S *Supporting Information*

ABSTRACT: We present a simple, bottom up method for the structural design of solid microparticles containing crystalline drug and excipient using microfluidic droplet-based processing. In a model system comprising 5-methyl-2-[(2-nitrophenyl)amino]-3-thiophenecarbonitrile (ROY) as the drug and ethyl cellulose (EC) as the excipient, we demonstrate a diversity of particle structures, with exquisite control over the structural outcome at the single-particle level. Within microfluidic droplets containing drug and excipient, tuning droplet composition and solvent removal rates allows us to controllably access structural diversity via an interplay of three physical processes (liquid–liquid phase separation, drug crystallization, and polymer vitrification) occurring during solvent removal. Specifically, we demonstrate two levels of structural control—a coarse "macro" particle structure and a finer "micro" structure. Further, we elucidate the key mechanistic elements responsible for the observed structural diversity using a combination of systematic experiments, thermodynamic arguments based on a three-component phase diagram, and dissipative particle dynamics simulations. We validate our method with two different excipient and drug combinations—ROY and poly(lactic-*co*-glycolic acid), and EC and carbamazepine (CBZ). Finally, we present preliminary investigations of in vitro drug release from two different types of CBZ–EC particles, highlighting how structural control allows the design of drug release profiles.
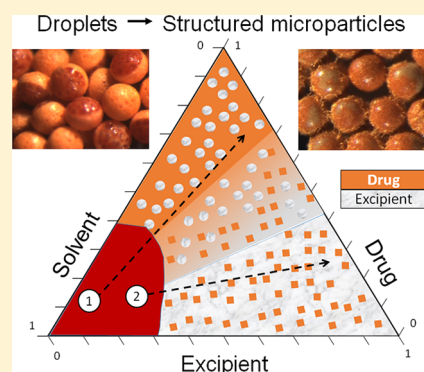
1. INTRODUCTION

The design, formulation, and manufacturing of engineered composites containing a *solid* active pharmaceutical ingredient (API) and polymeric excipient(s), with precisely tailored composition and structure, have been of tremendous academic and industrial interest in recent years for two primary reasons. First, from the perspective of pharmaceutical materials science and product design, engineered solid composites allow new and exciting possibilities in the creation of drug products with tailored dosage and release profiles.[1−5] Second, and equally importantly, such granular materials can have enhanced processability in terms of flow properties[6] and enable paradigm-shifting intensification (and simplification) of the traditional pharmaceutical manufacturing workflow, while also facilitating agile and decentralized supply chain models that can rapidly respond to evolving market forces.[7,8] In particular, the latter is made possible by the use of engineered composites as *intermediate* drug products, which can be converted to the final dose form on-demand with minimal further processing, in a customized and decentralized fashion. Recent demonstrations of solid drug-polymer composites include amorphous solid dispersions,[9] microparticles,[10,11] and hydrogels laden with the API in the crystalline form.[1]

This paper focuses on a recently developed technique that combines microfluidic generation of droplets carrying dissolved API (with or without dissolved excipient material), and evaporative crystallization/solidification in thin films, to produce monodisperse spherical microparticles of crystalline API coformulated with solid excipient in a "bottom up" fashion.[12,13] The formulation of both hydrophilic and hydrophobic drug molecules has been demonstrated using this technique. Interestingly, it has also been shown that the simultaneous solidification of hydrophobic drugs, such as 5-methyl-2-[(2-nitrophenyl)amino]-3-thiophenecarbonitrile (ROY) or carbamazepine (CBZ), with a polymeric excipient, such as ethyl cellulose (EC), not only enables shorter crystallization times, but also allows a remarkable degree of process-based selectivity over the polymorphic form of the
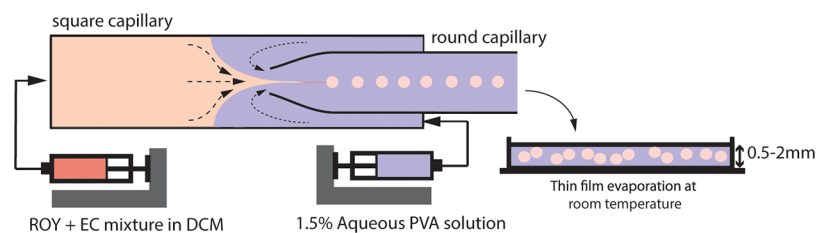
Figure 1. Experimental setup for the generation and collection of ROY–EC droplets into static thin films for evaporative solidification. Different initial solution compositions of ROY and EC were prepared in dichloromethane (DCM) and used as the dispersed phase. The continuous phase, a 1.5 wt % aqueous PVA solution, was introduced into a concentric glass capillary microfluidic device in a counter-flow configuration. Predispensed films of the continuous phase were prepared at varying thicknesses (of 0.5–2.0 mm) in collection dishes.

crystalline drug.[14] This method has the potential to be widely adopted as a simple method for single-step crystallization and direct compaction of drugs and excipients, which circumvents several energy intensive downstream steps in the pharmaceutical manufacturing workflow, while also allowing the creation of "designer" drug products with a hitherto unprecedented level of control over solid particle attributes.

These demonstrations notwithstanding, the complexity of the (at least) three-component drug–excipient–solvent system confined within microscale droplets, and the attendant complexity of the dynamic processes of phase separation and drug/excipient solidification that occur within the droplets,[15,16] make it challenging to develop *general* guidelines that allow a priori design of the structure and composition of these drug–excipient composites. Therefore, in this paper, we focus on a phenomenological study of the dynamics of simultaneous API/excipient solidification and structure formation within evaporating microfluidic emulsion droplets, in an attempt to delineate the basic and *general* elements of these processes.

In a model system comprising 5-methyl-2-[(2-nitrophenyl)-amino]-3-thiophenecarbonitrile (ROY) as the drug and ethyl cellulose (EC) as the excipient, we are able to demonstrate a diversity of particle structures, with exquisite control over the structural outcome at the single-particle level. Starting with microfluidic droplets containing drug and excipient dissolved in a common solvent, tuning droplet composition and solvent removal rates allows us to controllably access structural diversity via an interplay of the three physical processes (liquid–liquid phase separation, drug crystallization, and polymer vitrification) occurring within each droplet during solvent removal. Specifically, we demonstrate two levels of structural control—a coarse "macro" particle structure and a finer "micro" structure with our chosen model system. Further, we elucidate the key mechanistic elements responsible for the observed structural diversity using a combination of systematic experiments, thermodynamic arguments based on a three-component phase diagram, and dissipative particle dynamics (DPD) simulations. We validate our method by applying it to fabricate microparticles containing ROY and a different matrix material, poly(lactic-*co*-glycolic acid) (PLGA), and those comprising EC and a different drug, carbamazepine (CBZ). Finally, we present preliminary investigations of in vitro drug release from two different types of CBZ–EC particles, highlighting how structural control allows the design of drug release profiles.

2. EXPERIMENTAL SECTION

2.1. Materials. Poly(vinyl) alcohol (PVA) (M.W. 67,000), dichloromethane (DCM) (99.5%), ethyl cellulose (EC) (viscosity 10 cP), poly(lactic-*co*-glycolic acid) (PLGA) (50:50), and carbamazepine

(CBZ) were purchased from Sigma-Aldrich (Singapore) and used as received. 5-Methyl-2-[(2-nitrophenyl)amino]-3-thiophenecarbonitrile (ROY) was purchased from Nanjing Chemlin Chemical Industry Co. Ltd., China. Ultrapure water (18.3 MΩ) obtained using a Millipore Milli-Q purification system was used to prepare aqueous PVA solution. Harvard PHD 22/2000 series syringe pumps were used to dispense fluids into the emulsion generator. Square and cylindrical glass capillaries of I.D. 1 mm and 0.7 mm respectively were purchased from Arte Glass Associates Co. Ltd., Japan.

2.2. Methods. (i) Fabrication of drug-excipient microparticles: A glass capillary microfluidic setup for emulsion generation was assembled with square and cylindrical glass capillaries, as also reported previously.[14] First, the cylindrical glass capillary surfaces were rendered hydrophilic through treatment with oxygen plasma (100 W) for 120 s. Thereafter, the square and cylindrical glass capillary were assembled coaxially. The aqueous continuous phase (W) used was 1.5 wt % PVA in ultrapure water. The compositions of the dispersed phase (O) used in the synthesis of ROY–EC microparticles were set at ROY and EC concentrations of 120, 320, 420 mg/mL and 20, 40, 80 mg/mL of DCM respectively. For validation experiments, the dispersed phase for the synthesis of CBZ–EC microparticles, CBZ and EC concentrations were both set at a fixed mass ratio of 1 at either 40 or 60 mg/mL in DCM for the formation of janus and homogeneous particles, respectively. 3 wt % PVA in ultrapure water was used as the continuous phase in generating CBZ–EC. For the synthesis of ROY–PLGA microparticles, concentrations of ROY and PLGA were set at 120 mg/mL and 10, 100 mg/mL in DCM to form janus and homogeneous particles, respectively. W and O phases were infused from opposing ends of the square capillary with syringe pumps (Harvard PHD 22/2000), where the two phases contact at the tapered tip of the cylindrical glass capillary in a flow-focusing configuration (Figure 1). Flow rates for each phase were adjusted to obtain monodisperse emulsions in the size range of 150–300 μm. 5.1 and 5.7 cm I.D. glass wells were used for sample collection as well as solidification platforms.

These glass wells were prefilled with a film (0.5 mm or 2 mm thickness) of the aqueous phase prior to the collection of 100 μL of the dispersed phase. Excess continuous phase was removed after sample collection. Evaporative solidification was done at ambient conditions (24 °C and 55% humidity). The particles were washed with ultrapure water and vacuum-dried immediately after 2 h and 5 h, for the thin and thick film cases, respectively. The predispensed film was measured to be at 0.4 mm and 1.8 mm at the end the evaporative solidification, for the thin and thick film cases, respectively. For the formation of janus and homogeneous ROY–PLGA particles, a 4.0 mm and 0.5 mm film was implemented respectively (see above for the respective loadings in each case); the homogeneous particles exhibit a polymer-in-drug microstructure. A 2.0 mm film implemented for solidification of the same ROY–PLGA droplets (loaded at 120 and 10 mg/mL in DCM) gave a homogeneous macrostructure and drug-in-polymer microstructure (Figure 7). For the formation of janus and homogeneous CBZ–EC particles, a 2.0 mm and 0.5 mm film was implemented, respectively. (ii) In vitro release studies: 6 mg of dry CBZ-EC microparticles were weighed out and placed into a 250 mL glass jar filled with 100 mL of ultrapure water. The glass jar was sealed

with parafilm and placed firmly in a shaker set at 115 rpm. The release media absorbance was measured at 285 nm using a Shimadzu UV-1800 UV–vis spectrophotometer.[17] Samples were taken to monitor the release of carbamazepine over both short and long time scales. Measurements were made between 0–2 h at 20 min time intervals, from 2–4 h at 30 min intervals, from 4–10 h at hourly intervals, 10–120 h at 12 hourly intervals. 0.5 mL of solution was taken and replaced with fresh ultrapure water to maintain a constant buffer volume. A reference curve was also established using a series of standard solutions of carbamazepine dissolved in water at the following concentrations: 1.0, 5.0, 12.0, 18.0, 25.0, and 30.0 μg/mL. This reference curve was then used to calculate the amount of carbamazepine released at every interval. All dissolution sets were performed in triplicate.

2.3. Characterization. Optical microscopy images of the process and samples were captured using a Qimaging MicroPublisher 5.0 RTV camera mounted on an Olympus SZX7 microscope. A Leica CLS 150 XE light source was used for illumination. A field emission scanning electron microscope (JEOL JSM-6700F) at 5 kV accelerating voltage was used to acquire further structural information on the microparticles. All samples were prepared on conventional SEM stubs with carbon tape and were coated with ~10 nm of platinum by sputter coating. To reveal the cross sections of the microparticles, regular scotch tape was used to adhere and remove parts of the microparticles. Pore size distributions were obtained via digital image analysis (using ImageJ, NIH), in which 100 pores per region were measured from the cross sections of janus and homogeneous ROY-EC microparticles. The DSC thermograms were obtained using a Mettler Toledo DSC 882 apparatus. Around 5 mg of sample was crimped in a sealed aluminum pan and heated at 3 °C/min in the range of 100–225 °C using an empty sealed pan as a reference. Dry nitrogen was used as purge gas and the N_2 flow rate was 50 mL/min. The DSC instrument has a signal-to-noise ratio of ~12. Raman microscopic analysis was performed on the surface of ROY–EC microparticles using Renishaw inVia Raman spectrometer with a 514 nm laser (at a 20× objective with an accumulation time of 10 s). The curve resolution method used is the band-target entropy minimization (BTEM) algorithm.[18−20] The samples were scanned from 200 to 1800 cm^{-1}. Raman maps of 15 μm by 15 μm or 30 μm by 30 μm were obtained. Raman point-by-point mapping was performed on the mentioned area with a step size of 3.0 μm in both the x and y directions. The BTEM spectral estimates were then mapped back to the original data to obtain the spatial distributions of ROY. Raman measurements for the combined distribution of ROY across the maps are shown in Figure 2b,d, and pure component maps are shown in Figure S2 (see section 2 of the Supporting Information). The methodology of combining BTEM results with Raman maps and to obtain individual component spectral maps has been covered in earlier publications by Widjaja et al.[21,22]

3. RESULTS AND DISCUSSION

3.1. Phenomenology of Particle Structure. We first present the results of a series of experiments carried out on our chosen system system comprised of droplets of dichloromethane (DCM) containing 5-methyl-2-[(2-nitrophenyl)-amino]-3-thiophenecarbonitrile (ROY) as the model drug and ethyl cellulose (EC) as the excipient, dispersed in an aqueous medium containing water and a small amount of poly(vinyl alcohol) (PVA) as surfactant. The basic experimental scheme is provided in Figure 1. DCM droplets containing dissolved ROY and EC (at different compositions) were first generated in an aqueous continuous phase in a simple capillary-based microfluidic emulsion generator. After generation, the droplets were dispensed as a static monolayer (in fixed quantities) into small dishes containing a thin aqueous film and left undisturbed as the DCM solvent evaporated and left the droplets, ultimately yielding solid ROY–EC particles. This system was demonstrated in a previous study, where compact drug–excipient composites were obtained upon evaporative
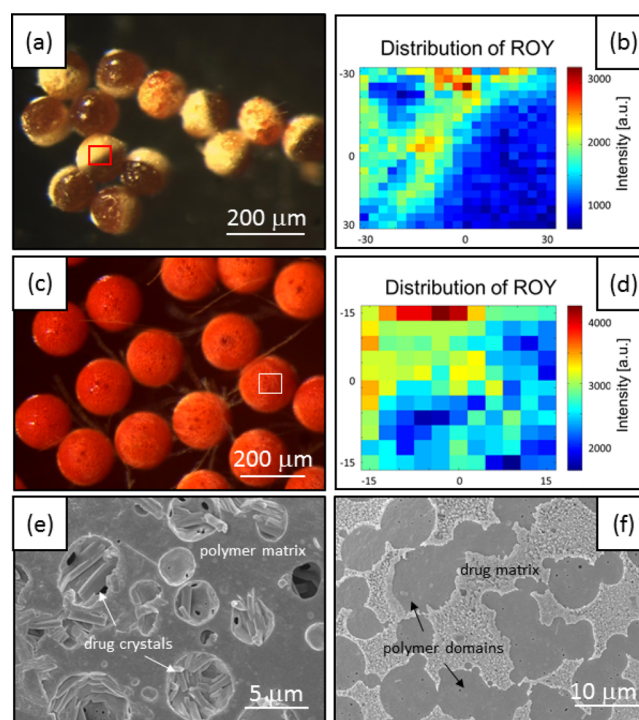

Figure 2. (a) Optical microscopy images of janus ROY–EC particles. (b) Spatial distribution of ROY across the color boundary in a janus particle (highlighted box in (a)); the distribution obtained across a 30 μm × 30 μm area using Raman spectroscopy reflects higher ROY content in one-half (the less porous region) of the particle. (c) Optical microscopy images of homogeneous ROY–EC particles. (d) Spatial distribution of ROY across the particle surface marked (highlighted box in (c)); the Raman map obtained across a 15 μm × 15 μm area shows no preferential segregation of ROY. FESEM images of the two observed microstructures: (e) Drug-in-polymer—white arrows point to clusters of drug crystals, and (f) Polymer-in-drug—black arrows indicate distinct smooth polymer domains embedded within a matrix of drug crystals.

solidification, lead to small drug crystals (<10 μm) dispersed within a solid EC matrix.[14] In the present set of studies, our main aim was to explore and ultimately understand, via a simple design-of-experiments scheme, the effect of two parameters—droplet composition and solvent removal rate—on the *structural* outcome of the solidification process. These parameters were previously studied in tuning the morphological outcome of *neat* crystalline glycine particles;[23] the presence of an added component—the excipient—in the current study adds another dimension of chemical and physical complexity, since *two* solidification processes need to be considered simultaneously, as discussed below.

We designed a set of experiments with monodisperse droplets within a narrow size range (150–300 μm mean size), at three levels of ROY and EC concentration, and conducted evaporative solidification of these droplets at two film thicknesses, to tune the solvent removal rates to nominally "high" and "low" levels. ROY and EC concentrations within the droplets were set at 120, 320, 420 mg/mL and 20, 40, 80 mg/mL respectively, well below the experimentally determined solubility of each molecule in DCM (ROY ≈ 580 mg/mL; EC ≈ 145 mg/mL respectively), so that all experiments started with undersaturated droplets. A fixed volume of droplets was collected as a monolayer in aqueous films of two different thicknesses at 0.5 mm and 2.0 mm, and the corresponding
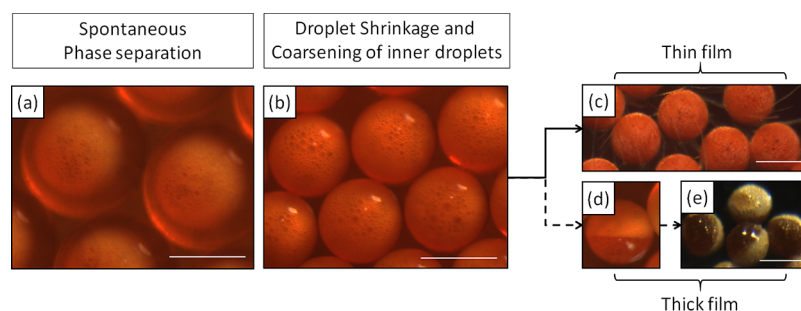
Figure 3. Optical microscopy images depicting the formation of ROY−EC particles from droplets via solvent evaporation. (a) Within seconds after dispensing emulsions into the aqueous thin film, spontaneous phase separation leads to formation of a dispersion of smaller droplets within each droplet. (b) Subsequent solvent removal leads to droplet shrinkage and coarsening of the dispersion of inner droplets. (c) Homogeneous particles obtained upon solvent removal in thin (∼0.5 mm) films. (d) Settling of the coarsening inner droplet dispersion, during slow evaporation in thicker films (∼2 mm), leads to the evolution of a distinctly janus structure, as seen in this optical microscope image of a droplet turned on its side, where the darker hemisphere contains the denser phase. (e) Janus ROY-EC microparticle obtained upon complete solvent removal from droplets of the kind shown in (d). Also see images in Figure 2a,c for further examples of the two broad macrostructures obtained. All scale bars represent 300 μm.
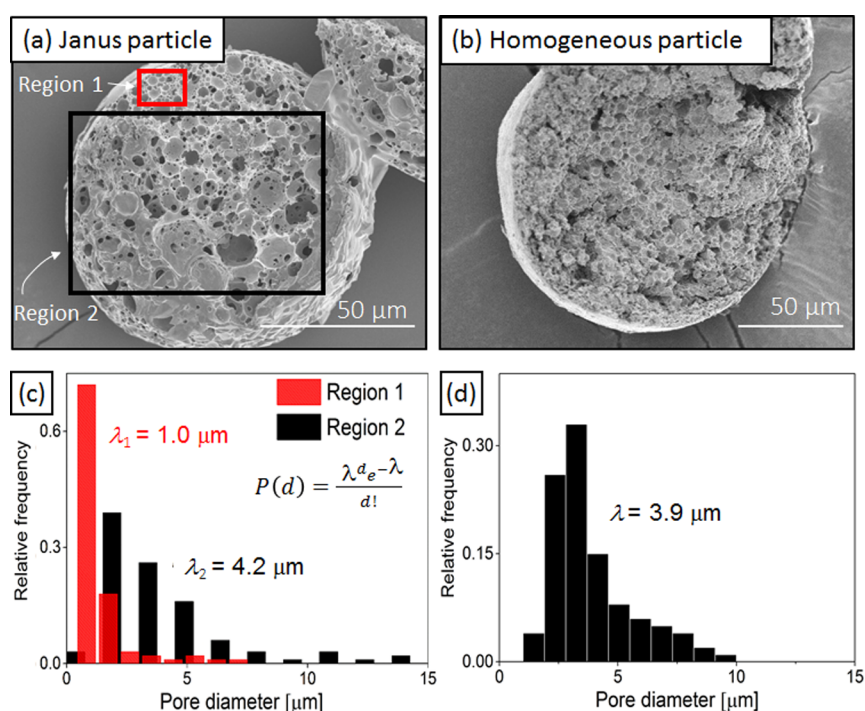

Figure 4. Representative SEM images of cross sections of (a) janus, and (b) homogeneous structured ROY−EC microparticles. Pore size distributions via digital image analysis (ImageJ, NIH) of the (c) janus microparticle across Regions 1 and 2 as marked out in (a), and (d) of the homogeneous particle; d represents the pore diameter, and λ is the mean pore diameter.

experimentally observed times for complete solidification were ∼2 h and ∼5 h respectively for these two cases, at all droplet compositions.

Figure 2 is a summary of the key results from these experiments, from the standpoint of particle structure. Interestingly, we observed *two* levels of structural control over the resultant solid particles—a coarse "macro" particle structure and a finer "micro" structure, with two possibilities in each case, leading to *four* combinations of observed particle structure. In general, a faster rate of solvent removal (i.e., in the thinner 0.5 mm film) and higher drug and polymer concentrations generally favored the formation of homogeneous spherical particles, in that the coarse structure was spatially uniform across the particle (Figure 2c). On the other hand, it was observed that slow rates of solvent removal (i.e., in the thicker 2 mm film) and low to moderate drug and polymer

concentrations led to the formation of "janus" spherical particles, characterized by particles displaying two distinct halves of different colors (Figure 2a). Further, spatial chemical analysis via Raman microscopy measurements (Figure 2b,d) also revealed that the janus particles exhibited difference in drug content across the two halves of the particle. Finally, the macrostructural outcome was *specific*, in that nearly all particles in a given experimental ensemble displayed the same macrostructure. In addition, we also observed two classes of finer scale microstructure within the particles, regardless of the macrostructure obtained. In the first class of fine structure, ROY crystals were embedded within small pockets on the particle surface or within the interior, presumably surrounded by solidified EC—a structure we term *"drug-in-polymer"* (Figure 2e). In contrast, we also observed cases of the opposite structure, in which distinct and smooth EC domains were

found embedded within a matrix composed of tightly packed drug microcrystals; we refer to this as the *"polymer-in-drug"* fine structure (Figure 2f).

In the following sections, we analyze this structural diversity in terms of an interplay between three physical processes: liquid−liquid phase separation, drug crystallization, and polymer vitrification—occurring within each droplet during solvent removal.

3.2. Phenomenology of Solidification Dynamics. After describing the diversity of final particle structures obtained in our experiments, we now summarize our observations of the dynamic processes occurring within each droplet during evaporative solidification, which were common across all experimental conditions. The typical time evolution of droplets, as they gradually lose solvent (DCM), is shown in Figure 3.

The first observation, as also reported previously,[14] was that of spontaneous and rapid liquid−liquid phase separation within each droplet, which yielded a dispersion of small liquid droplets (∼1−10 μm) dispersed within each individual droplet, which coarsened with time. Such (thermodynamic) phase separation is commonly observed in solutions of pure drug/polymer in solvent,[24−28] as well as in drug−polymer mixtures in a common solvent,[29] and is an outcome of partial miscibility between the drug/polymer and solvent beyond certain threshold concentrations.[29−31] We conducted a series of macroscale batch experiments on liquid−liquid phase separation (see Section 3 and Figure S3 of Supporting Information), which indicated that the phase separation was triggered by the presence of the aqueous continuous phase and led to the formation of a DCM-rich minority phase and a bulk phase rich in both ROY and EC. We return to this issue in Section 3.4 below. Interestingly, analysis of SEM images of the *final* particle structure provided further insight into the compositions of the two liquid phases formed within all droplets after phase separation in the early stages. We observed a highly porous internal particle structure under all experimental conditions (Figure 4a,b); the empty pores suggesting that the DCM acts as a porogen, in turn implying that the inner droplets formed after phase separation were lean in both ROY and EC, and were surrounded by a continuous fluid rich in both ROY and EC, which ultimately solidified upon further evaporation of DCM, via both polymer vitrification (upon crossing the glass transition concentration) and drug crystallization (upon crossing the saturation threshold).

3.3. A General Hypothesis for the Evolution of Particle Macrostructure. Given the above observation of particle structures and solidification dynamics, we arrive at our first general hypothesis, which explains particle macrostructure as the outcome of the competition between coarsening and settling of the DCM-rich (and therefore denser) inner droplets and solidification of the outer, ROY−EC-rich fluid. Generally, at high solute concentrations and fast solvent removal rates (in thin films), solidification is able to prevent coarsening and settling of inner droplets, which ultimately lose DCM and become hollow pores uniformly distributed within the particles. This hypothesis is supported by three clear pieces of evidence from our experiments. First, droplet ensembles of identical compositions but solidified under different film thicknesses showed a clear macrostructural trend toward janus structures for *thick* films and homogeneous structures for *thin* films, in which solvent is removed rapidly. Second, further analysis of SEM images of the janus particles revealed a gradient of porosity across the two halves of the particle (Figure 4a,c), with

large pores (of mean pore diameter ∼4.2 μm) aggregating in one-half and small pores (of mean pore diameter ∼1.0 μm) in the other; this was also responsible for the different observed colors for the two halves, under optical microscopy (see Figure 2a). These two observations reveal that given enough time (before the onset of solidification), settling of the coarsening suspension of inner droplets will lead to a size sorting process within each large droplet, leading ultimately to a porosity gradient in the final microparticles. Finally, and more subtly, homogeneous structures were formed at all ROY concentrations used, when the EC concentration exceeded a threshold that was film thickness dependent (40 and 80 mg/mL for the thin and thick film cases respectively). Increasing EC concentration, even at low ROY concentrations, leads to rapid viscosification of the ROY-EC-rich outer fluid within the droplets, thereby retarding the settling of inner droplets, and also accelerating vitrification of the outer fluid, which ultimately arrests the inner droplet positions, thus leading to homogeneous structures. The pores across these particles were spatially homogeneous, with mean pore diameter of ∼3.9 μm (Figure 4b,d). Interestingly, the pore size distributions (PSDs) follow Poissonian statistics for both cases of macrostructure. This suggests that a coalescence driven mechanism in which successive coalescence events are nominally independent of each other, leading to evolution of the PSDs from exponential decays (Region 1 in Figure 4c) to skewed distributions with extended tails (Region 2 in Figure 4c,d). In all cases, we also observed that the onset of crystallization occurred when most of the DCM had been removed and the contents within the droplet reached a viscous melt-like state, which counteracted the effect of crystal density and prevented further segregation and settling.[12]

3.4. A Phase Diagram Perspective on the Evolution of Particle Microstructure. As discussed in Section 3.2, we observe spontaneous phase separation within the droplets, which leads to a (i) DCM-rich liquid phase, which ultimately develops into empty microscale pores, and a (ii) phase rich in ROY and EC, which solidifies into the different microstructures of Figure 2. This latter phase, rich in ROY and EC, is initially very close to the starting composition within the droplets, as demonstrated in Section 3 and Figure S3 of the Supporting Information. Next, we develop a ternary ROY−EC−DCM phase diagram for the ROY and EC-rich phase, based on mass fractions of the three major components, with the help of which we can further elucidate the various phase transition and solidification processes occurring while the droplets lose solvent. We neglect the presence of water in this phase, since it is a minority component (<0.1% w/v).[32] The aim of such a description is to explain and ultimately predict the structural outcome given only information about the starting composition of the droplets.

The experimentally measured solubilities of ROY and EC in DCM are used to demarcate a liquid zone in the phase diagram (Figure 5), outside which both drug and excipient are supersaturated. We also demarcate a metastable zone, the outer boundary of which is assumed to lie at ∼2 times the respective solubilities of the two solutes; outside this metastable zone lies the solid zone, in which either ROY or EC (or both) are assumed to spontaneously crystallize/vitrify. Within the metastable zone, ROY is supersaturated, and there is therefore a finite possibility of crystal nucleation and growth.[33] Likewise, EC undergoes a liquid-to-gel transition in this zone, and ultimately transitions into a glassy vitrified state outside it.[31]
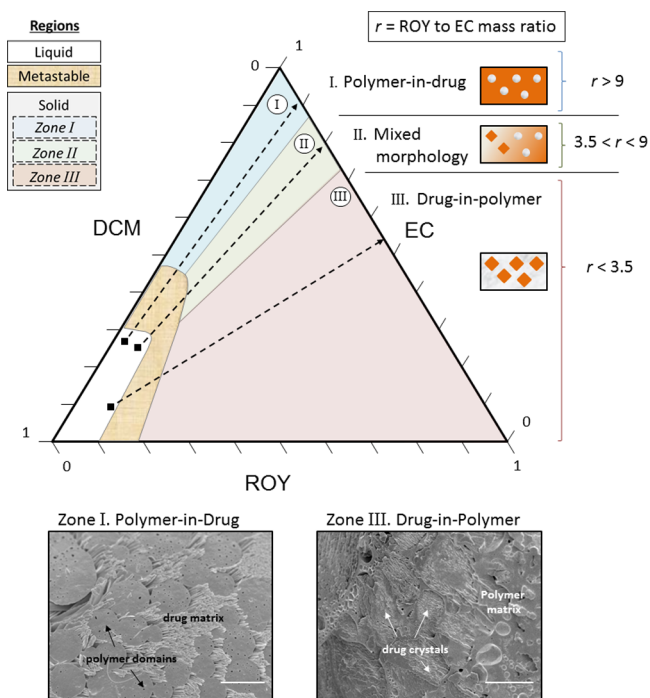
Figure 5. Ternary ROY–EC–DCM phase diagram with shaded regions corresponding to liquid, metastable, and solid states, respectively. Three different initial compositions of the ROY and EC-rich phase are indicated by black squares (■) in the liquid zone of the phase diagram. The dotted lines indicate subsequent trajectories of these points across the phase diagram as the DCM evaporates; three different microstructures are possible, as indicated, based on this traversal of the phase diagram. Also provided are FESEM images of the respective microstructures for Zones I and III. All scale bars represent 10 μm.

Three solid zones outside the metastable zone are marked in Figure 5. Our experimental observations indicate that the ROY-to-EC mass ratio r in the droplets can be directly related to the eventual particle microstructure; the three zones are demarcated by lines of constant r, with the experimentally determined boundaries lying at $r = 3.5$ and $r = 9$ respectively.

Points within Zone I represent states of the system where ROY has crossed its solubility threshold while EC has not; likewise, all points lying within Zone III represent the corresponding states of the system where EC has crossed its solubility threshold while ROY has not. Zone II indicates a territory on the phase diagram corresponding to states in which *both* ROY and EC have crossed their respective solubility thresholds. We also note that the ROY concentrations used in all experiments are above its solubility in ethyl cellulose, which leads to the formation of separate crystalline drug and amorphous polymer domains, instead of homogeneous amorphous solid dispersions.[30]

Three representative starting compositions of the ROY and EC-rich phase within the liquid zone are depicted in Figure 5. Dotted lines indicating trajectories followed by the ROY and EC-rich phase across the phase diagram are shown, along which different sequences of solidification processes are possible, depending on the initial position on the phase diagram. The trajectories are drawn on the basis of two simple assumptions: (i) that only DCM is lost as the evaporation proceeds to completion, while the ROY and EC masses (and therefore the ROY-to-EC mass ratio r) are conserved, and (ii) the solvent removal occurs in a quasi-static manner, so that every point along the trajectory is assumed to be at equilibrium. The trajectories are therefore also lines of constant r, similar to the zone boundaries drawn on the diagram. At mass ratios $r > 9$, the trajectories pass through Zone I, where ROY has crossed its solubility threshold, and therefore crystallizes prior to the vitrification of EC, thus implying that the microscale structure is predominantly the polymer-in-drug type described in Section 3.1. Conversely, at low mass ratios $r < 3.5$, the trajectory passes through Zone III, and implies that EC vitrification precedes that of ROY, thus implying that the microscale structure is predominantly the drug-in-polymer type also described in Section 3.1. For intermediate ROY to EC ratios ($3.5 < r < 9$), the system crosses over to Zone II, where drug crystallization and polymer vitrification can occur simultaneously, leading to the presence of both possible microstructures within each particle.
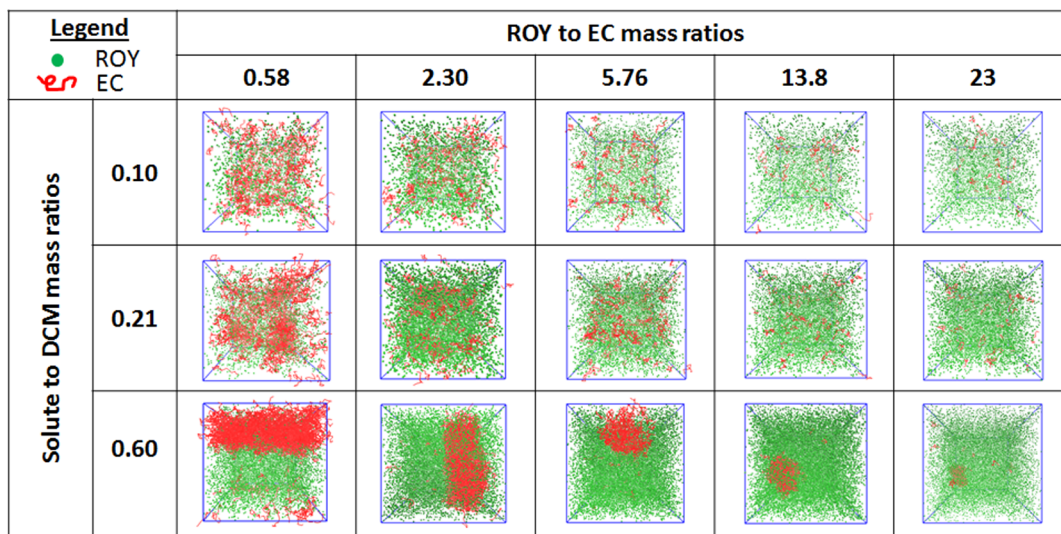

Figure 6. Results from DPD simulations indicating the spatial segregation of ROY and EC at varying ROY-to-EC mass ratios, and solute (ROY + EC) to DCM mass ratios.

3.5. Insights from Dissipative Particle Dynamics (DPD) simulations. To gain further insight into the various molecular interactions in our three-component system, we conducted a series of molecular and dissipative particle dynamics (DPD) simulations as described below (full details on simulation set up may be found in Section 4 of the Supporting Information). The solubility parameters of ROY and EC were first calculated using molecular dynamics simulations, based on a methodology developed by Gupta et al.,[34] to be 21.3 and 14.8 MPa$^{1/2}$ respectively, indicating borderline miscibility.[35] We then conducted coarse-grained dissipative particle dynamics (DPD) simulations, where the DPD interaction parameters were obtained from the calculated solubility parameters.[36] DPD simulation methods have previously been used in modeling phase separation of binary polymer mixtures,[37] microphase separation in diblock copolymer systems,[38] and micelle formation of copolymer systems in aqueous solution.[39] We examined ROY-to-EC mass ratios ranging between 0.58−23, and DCM-to-solute (ROY + EC) mass ratios between 0.1−0.6, to mimic the traversal of the three component phase diagram from different starting compositions. Our simulations revealed a clear trend toward spatial segregation of EC and ROY molecules from each other with decreased DCM content at all ROY-to-EC mass ratios studied, as shown in Figure 6. The observed segregation is due to the borderline miscibility of EC and ROY, and similar phase behavior has been reported for indomethacin in sucrose.[34,35] This spatial segregation at the scale of our simulations, which was carried out in cubes of ~30 nm, lends support to the hypothesis of microstructure development described in Section 3.4 above. The segregated liquid phases eventually coarsen and solidify upon sufficient supersaturation into the corresponding solids in either the polymer-in-drug or drug-in-polymer structure.

3.6. Method Validation and in Vitro Drug Release Studies for Janus and Homogeneous Microparticles. Finally, as a proof of concept, we demonstrate structural control for two different drug−excipient systems: ROY-poly(lactic-co-glycolic acid) (PLGA) and carbamazepine-ethyl cellulose (CBZ−EC). For ROY−PLGA microparticles, we successfully fabricated both janus and homogeneous macrostructures, and for the homogeneous case, we were further able to tune the internal microstructure to both polymer-in-drug and drug-in-polymer morphologies upon varying the process parameters in line with the discussions presented above (Figure 7a−d). Similarly, by varying CBZ and EC loadings and film thicknesses, we designed janus and homogeneous structured CBZ−EC microparticles (Figure 7e,f). The detailed experimental conditions are provided in Section 2.

Finally, we conducted drug release studies over 5 days on the two types of CBZ−EC microparticles, to evaluate the extent to which the structure affects drug release in this case. A drug-to-excipient mass ratio of 1 was used in fabricating both particle microstructures, and the same polymorphic form was obtained, as verified by differential scanning calorimetry (DSC) measurements (see Supporting Information, Figure S1). Figure 8a,b shows the obtained long-term and short-term release profiles respectively; both janus and homogeneous microparticles generally exhibit profiles of similar shapes, but the janus particles have a slower dissolution rate than their homogeneous counterparts. Fitting the classic Weibull model to the measurements revealed that the release does not follow simple first order kinetics ($b = 1$); the b exponent in the model was approximately 0.5 for both cases, suggesting that the release is
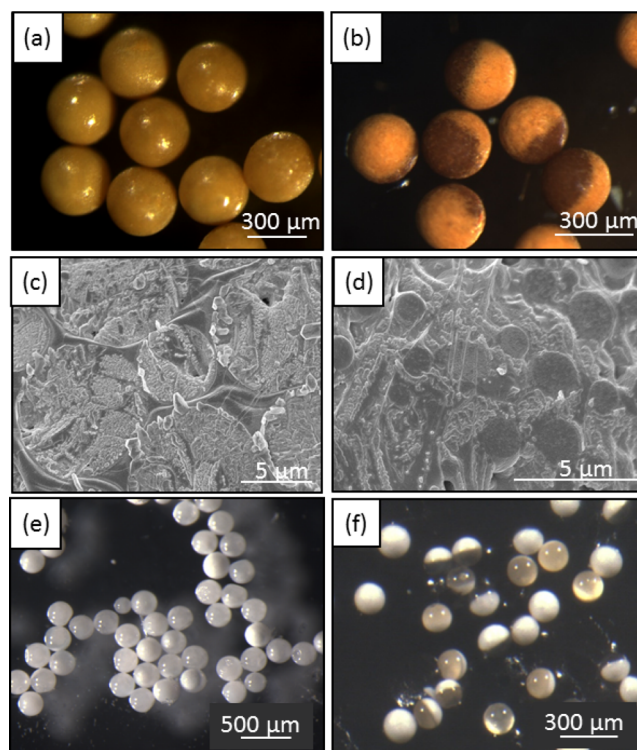
Figure 7. Optical microscopy images of ROY−PLGA particles, with (a) homogeneous structure and (b) janus structure. FESEM images of (c) polymer-in-drug microstructure observed on the surface of the homogeneous particles in panel a, and drug-in-polymer microstructure on the surface of a different set of ROY−PLGA microparticles (also homogeneous in macrostructure). Optical microscopy images of CBZ−EC microparticles with (e) homogeneous structure, and (f) janus structure.

diffusion limited.[40] Crucially, the janus particles released drug with a characteristic time nearly double that of the homogeneous particles, highlighting the importance and relevance of particle structure to the in vitro release profile.

This doubling of characteristic release time may be attributed to the distinct differences in porosity between the janus and homogeneous particles, as discussed in Section 3.3 above. Briefly, the homogeneous particles exhibited a uniform porosity distribution, while the janus particles exhibited a spatially segregated porosity profile with two distinct scales of porosity in the two halves. Now, the *extent* to which porosity at different scales affects the drug release depends on how *interconnected* the various sized pores are within the particle. If the smaller, submicron pores are well distributed ("mixed") amidst the micrometer-scale pores, as in the homogeneous particles, then their respective resistances to diffusion of the drug act in parallel, and the drug release is mainly controlled by diffusion through the *larger* pores, which offer the least resistance. Figure 9 presents a set of SEM images of the CBZ−EC particles pre- and postrelease. Figure 9a,c are prerelease SEM images for the homogeneous and janus particles, respectively; crystalline drug is homogeneously distributed throughout the former, while it is localized in the compact, nonporous half of the latter. Next, Figure 9b,d−e illustrates the residual porosity after the dissolution and release of the trapped drug crystals. The submicron scale residual porosity in the compact half of the janus particles is apparent in Figure 9d and poses a higher diffusional resistance to drug release, hence the longer
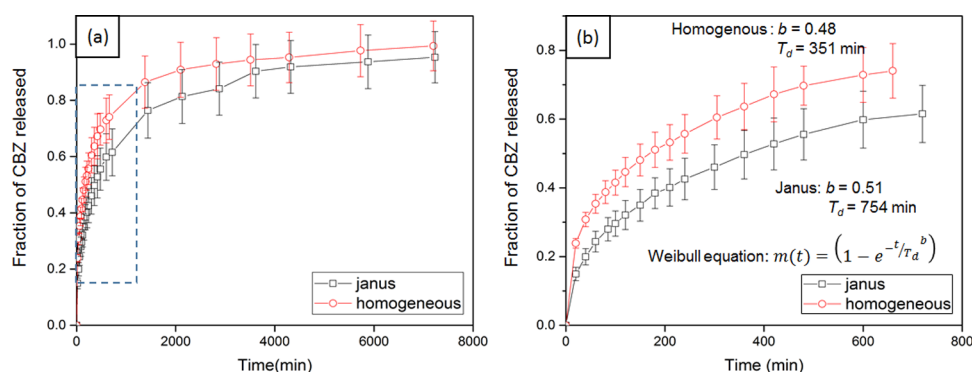
Figure 8. (a) Drug release profiles for janus and homogeneous CBZ−EC microparticles. The dotted inset marks out the short-term drug release (∼800 min duration), which is magnified in (b) for clarity. The Weibull model was fitted to the data, where $m(t)$ is the normalized fraction of CBZ released with time, and T_d is a characteristic time for 63.2% of drug to be released. The Weibull b exponent for both types of particles is found to be ∼0.5.
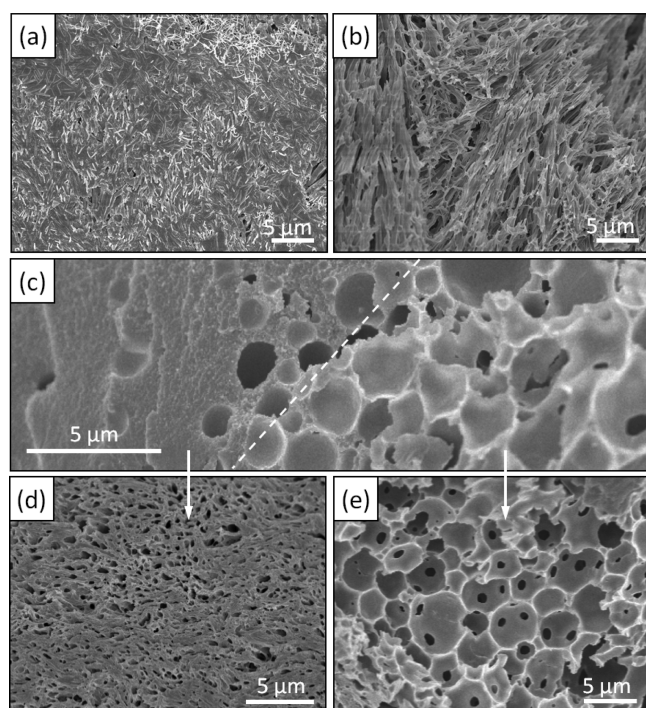

Figure 9. SEM images of cross sections of homogeneous CBZ−EC particles: (a) prerelease, (b) postrelease, and janus particles (c) prerelease. SEM images capturing the differences in porosity in the two halves of the janus particles postrelease: (d) submicron pore region and (e) microscale pore region, as also discussed in Section 3.3 (and Figure 4) above.

characteristic release time than the homogeneous particles with more even initial distribution of the drug. Finally, while we did not study drug release studies for particles with polymer-in-drug microstructures, we expect different release kinetics, since it is the drug that composes the "matrix" of the particle; in such a scenario, the drug would be released at a sustainably high rate, as opposed to the inverse drug-in-polymer case, where the drug release at later times is limited by diffusion through the pores of the polymer matrix. Further detailed experimental and theoretical studies on drug release kinetics from these different particle structures are out of the scope of the present work and are the topic of ongoing investigations.

4. CONCLUSION

In summary, we have presented a detailed phenomenological study of multiscale structural design of drug−excipient microparticles using microfluidic droplet generation and subsequent evaporative solidification in thin films. Using the ROY−EC system as a prototype, by modulating the solvent removal rates and droplet compositions we control the interplay between the key physical processes in play during particle formation, leading to controlled, predictable and different morphological outcomes in the final solid particles. On the basis of this understanding, we extended the technique to fabricate ROY−PLGA and CBZ−EC microparticles with different tunable macro- and microstructures. Finally, we conducted in vitro drug release measurements from CBZ−EC microparticles with different macrostructures and found that the structural differences led to measurable differences in CBZ release kinetics. Overall, this work sheds light on the complex dynamics of particle formation from droplets containing multicomponent mixtures and suggests a method for manipulating process parameters for structural control at the single particle level. The concepts from this work are generalizable to a diversity of drug-excipient composites, for the rational engineering of novel particulate constructs with varied spatial distributions of drug(s), and hence tailored drug release profiles. Combining ideas from the thermodynamic phase behavior of multicomponent systems,[41−43] and predictions of drug−polymer interactions from dissipative particle dynamics simulations and classical theories (such as Flory−Huggins theory),[44] it is now possible to envision general algorithms for the rational design and manufacturing of such multiscale drug composites. Furthermore, the mechanisms of drug release from such composites are interesting in their own right and are the topic of ongoing work beyond this study.

■ ASSOCIATED CONTENT

ⓈSupportingInformation

The Supporting Information is available free of charge on the ACS Publications website at DOI: 10.1021/acs.cgd.6b01701.

  1. Polymorphic characterization of CBZ-EC particles used for in vitro drug release. 2. Pure component BTEM spectra for ROY. 3. Batch liquid−liquid equilibrium experiments. 4. Details of molecular simulations (PDF)

■ AUTHOR INFORMATION

Corresponding Author

*E-mail: saifkhan@nus.edu.sg.

ORCID

Ammu Prhashanna: 0000-0002-9119-7552

Ambika Somasundar: 0000-0001-8545-0323

Qisong Xu: 0000-0002-1337-543X

Saif A. Khan: 0000-0002-7879-6147

Notes

The authors declare no competing financial interest.

■ ABBREVIATIONS

API, active pharmaceutical ingredient; ROY, 5-methyl-2-[(2-nitrophenyl)amino]-3-thiophenecarbonitrile; EC, ethyl cellulose; CBZ, carbamazepine; PLGA, poly(lactic-*co*-glycolic acid); DCM, dichloromethane; PVA, poly(vinyl alcohol); PSD, pore size distribution; DPD, dissipative particle dynamics; I.D., inner diameter; r, mass ratios of ROY to EC concentrations; t, time elapsed after dispensing emulsions, time elapsed from start of in vitro drug release; $m(t)$, normalized fraction of CBZ released from ROY-EC particles as a function of time; T_d, characteristic time interval for 63.2% of drug to be released; b, exponent in Weibull model; BTEM, band-target entropy minimization

■ REFERENCES

(1) Eral, H. B.; López-Mejías, V.; O'Mahony, M.; Trout, B. L.; Myerson, A. S.; Doyle, P. S. Biocompatible alginate microgel particles as heteronucleants and encapsulating vehicles for hydrophilic and hydrophobic drugs. *Cryst. Growth Des.* **2014**, *14*, 2073−2082.

(2) Li, J. K.; Wang, N.; Wu, X. S. A novel biodegradable system based on gelatin nanoparticles and poly (lactic-co-glycolic acid) microspheres for protein and peptide drug delivery. *J. Pharm. Sci.* **1997**, *86*, 891−895.

(3) Li, X.; Zhou, L.; Wei, Y.; El-Toni, A. M.; Zhang, F.; Zhao, D. Anisotropic growth-induced synthesis of dual-compartment Janus mesoporous silica nanoparticles for bimodal triggered drugs delivery. *J. Am. Chem. Soc.* **2014**, *136*, 15086−15092.

(4) Badruddoza, A. Z.; Godfrin, P. D.; Myerson, A. S.; Trout, B. L.; Doyle, P. S. Core-Shell Composite Hydrogels for Controlled Nanocrystal Formation and Release of Hydrophobic Active Pharmaceutical Ingredients. *Adv. Healthcare Mater.* **2016**, *5*, 1960−8.

(5) Wu, J.; Zhao, X.; Yeung, K. W. K.; To, M. K. T. Interfacial Fast Release Layer in Monodisperse Poly (Lactic-Co-Glycolic Acid) Microspheres Accelerates the Drug Release. *Curr. Drug Delivery* **2016**, *13*, 720.

(6) Kawashima, Y.; Okumura, M.; Takenaka, H.; Kojima, A. Direct preparation of spherically agglomerated salicylic acid crystals during crystallization. *J. Pharm. Sci.* **1984**, *73*, 1535−1538.

(7) Mascia, S.; Heider, P. L.; Zhang, H.; Lakerveld, R.; Benyahia, B.; Barton, P. I.; Braatz, R. D.; Cooney, C. L.; Evans, J.; Jamison, T. F.; et al. End-to-End Continuous Manufacturing of Pharmaceuticals: Integrated Synthesis, Purification, and Final Dosage Formation. *Angew. Chem., Int. Ed.* **2013**, *52*, 12359−12363.

(8) Adamo, A.; Beingessner, R. L.; Behnam, M.; Chen, J.; Jamison, T. F.; Jensen, K. F.; Monbaliu, J.-C. M.; Myerson, A. S.; Revalor, E. M.; Snead, D. R.; et al. On-demand continuous-flow production of pharmaceuticals in a compact, reconfigurable system. *Science* **2016**, *352*, 61−67.

(9) Brough, C.; Williams, R. Amorphous solid dispersions and nano-crystal technologies for poorly water-soluble drug delivery. *Int. J. Pharm.* **2013**, *453*, 157−166.

(10) Hombreiro Perez, M. H.; Zinutti, C.; Lamprecht, A.; Ubrich, N.; Astier, A.; Hoffman, M.; Bodmeier, R.; Maincent, P. The preparation and evaluation of poly (ϵ-caprolactone) microparticles containing both a lipophilic and a hydrophilic drug. *J. Controlled Release* **2000**, *65*, 429−438.

(11) Xu, Q.; Hashimoto, M.; Dang, T. T.; Hoare, T.; Kohane, D. S.; Whitesides, G. M.; Langer, R.; Anderson, D. G. Preparation of monodisperse biodegradable polymer microparticles using a micro-fluidic flow-focusing device for controlled drug delivery. *Small* **2009**, *5*, 1575−1581.

(12) Toldy, A. I.; Badruddoza, A. Z. M.; Zheng, L.; Hatton, T. A.; Gunawan, R.; Rajagopalan, R.; Khan, S. A. Spherical crystallization of glycine from monodisperse microfluidic emulsions. *Cryst. Growth Des.* **2012**, *12*, 3977−3982.

(13) Leon, R. A.; Wan, W. Y.; Badruddoza, A. Z. M.; Hatton, T. A.; Khan, S. A. Simultaneous spherical crystallization and co-formulation of drug (s) and excipient from microfluidic double emulsions. *Cryst. Growth Des.* **2014**, *14*, 140−146.

(14) Leon, R. A.; Badruddoza, A. Z. M.; Zheng, L.; Yeap, E. W.; Toldy, A. I.; Wong, K. Y.; Hatton, T. A.; Khan, S. A. Highly selective, kinetically driven polymorphic selection in microfluidic emulsion-based crystallization and formulation. *Cryst. Growth Des.* **2015**, *15*, 212−218.

(15) El-Banna, H. M. Solid dispersion of pharmaceutical ternary systems I: Phase diagram of aspirin-acetaminophen-urea system. *J. Pharm. Sci.* **1978**, *67*, 1109−1111.

(16) Chiou, W. L.; Riegelman, S. Preparation and dissolution characteristics of several fast-release solid dispersions of griseofulvin. *J. Pharm. Sci.* **1969**, *58*, 1505−1510.

(17) Carbamazepine Tablets. In *The United States Pharmacopeial Convention*, Nov 20, 2015; Vol. USP 39-NF 34.

(18) Widjaja, E.; Li, C.; Garland, M. Semi-batch homogeneous catalytic in-situ spectroscopic data. FTIR spectral reconstructions using band-target entropy minimization (BTEM) without spectral preconditioning. *Organometallics* **2002**, *21*, 1991−1997.

(19) Chew, W.; Widjaja, E.; Garland, M. Band-target entropy minimization (BTEM): an advanced method for recovering unknown pure component spectra. Application to the FTIR spectra of unstable organometallic mixtures. *Organometallics* **2002**, *21*, 1982−1990.

(20) Widjaja, E.; Li, C.; Chew, W.; Garland, M. Band-target entropy minimization. A robust algorithm for pure component spectral recovery. Application to complex randomized mixtures of six components. *Anal. Chem.* **2003**, *75*, 4499−4507.

(21) Widjaja, E.; Garland, M. Use of Raman microscopy and band-target entropy minimization analysis to identify dyes in a commercial stamp. Implications for authentication and counterfeit detection. *Anal. Chem.* **2008**, *80*, 729−733.

(22) Widjaja, E.; Lim, G. H.; Lim, Q.; Mashadi, A. B.; Garland, M. Pure component Raman spectral reconstruction from glazed and unglazed Yuan, Ming, and Qing shards: a combined Raman microscopy and BTEM study. *J. Raman Spectrosc.* **2011**, *42*, 377−382.

(23) Toldy, A. I.; Zheng, L.; Badruddoza, A. Z. M.; Hatton, T. A.; Khan, S. A. Dynamics and Morphological Outcomes in Thin-Film Spherical Crystallization of Glycine from Microfluidic Emulsions: Experimental Studies and Modeling. *Cryst. Growth Des.* **2014**, *14*, 3485−3492.

(24) Robinson, D. Ethyl cellulose-solvent phase relationships relevant to coacervation microencapsulation processes. *Drug Dev. Ind. Pharm.* **1989**, *15*, 2597−2620.

(25) Singh, A.; Lee, I. S.; Myerson, A. S. Concomitant crystallization of ROY on patterned substrates: Using a high throughput method to improve the chances of crystallization of different polymorphs. *Cryst. Growth Des.* **2009**, *9*, 1182−1185.

(26) Veesler, S.; Revalor, E.; Bottini, O.; Hoff, C. Crystallization in the presence of a liquid-liquid phase separation. *Org. Process Res. Dev.* **2006**, *10*, 841−845.

(27) Kong, T.; Liu, Z.; Song, Y.; Wang, L.; Shum, H. C. Engineering polymeric composite particles by emulsion-templating: thermodynamics versus kinetics. *Soft Matter* **2013**, *9*, 9780−9784.

(28) Min, N. G.; Kim, B.; Lee, T. Y.; Kim, D.; Lee, D. C.; Kim, S.-H. Anisotropic microparticles created by phase separation of polymer blends confined in monodisperse emulsion drops. *Langmuir* **2015**, *31*, 937−943.

(29) Ilevbare, G. A.; Taylor, L. S. Liquid−liquid phase separation in highly supersaturated aqueous solutions of poorly water-soluble drugs: Implications for solubility enhancing formulations. *Cryst. Growth Des.* **2013**, *13*, 1497−1509.

(30) Huang, Y.; Dai, W.-G. Fundamental aspects of solid dispersion technology for poorly soluble drugs. *Acta Pharm. Sin. B* **2014**, *4*, 18−25.

(31) Van de Witte, P.; Dijkstra, P.; Van den Berg, J.; Feijen, J. Phase separation processes in polymer solutions in relation to membrane formation. *J. Membr. Sci.* **1996**, *117*, 1−31.

(32) Davies, W.; Jaggeh, J.; Whalley, H. Methylene dichloride and 1:2-dichloroethane. I. Solubility of water. II. Vapour pressure. *J. Soc. Chem. Ind., London* **1949**, *68*, 26−31.

(33) Myerson, A. S.; Ginde, R. 2. Crystals, crystal growth, and nucleation. In *Handbook of Industrial Crystallization*, 2nd ed.; Butterworth-Heinemann: Woburn, 2002; pp 33−65.

(34) Gupta, J.; Nunes, C.; Vyas, S.; Jonnalagadda, S. Prediction of solubility parameters and miscibility of pharmaceutical compounds by molecular dynamics simulations. *J. Phys. Chem. B* **2011**, *115*, 2014−2023.

(35) Forster, A.; Hempenstall, J.; Tucker, I.; Rades, T. Selection of excipients for melt extrusion with two poorly water-soluble drugs by solubility parameter calculation and thermal analysis. *Int. J. Pharm.* **2001**, *226*, 147−161.

(36) Groot, R. D.; Warren, P. B. Dissipative particle dynamics: Bridging the gap between atomistic and mesoscopic simulation. *J. Chem. Phys.* **1997**, *107*, 4423.

(37) Liu, H.; Qian, H.-J.; Zhao, Y.; Lu, Z.-Y. Dissipative particle dynamics simulation study on the binary mixture phase separation coupled with polymerization. *J. Chem. Phys.* **2007**, *127*, 144903.

(38) Li, X.; Guo, J.; Liu, Y.; Liang, H. Microphase separation of diblock copolymer poly (styrene-b-isoprene): A dissipative particle dynamics simulation study. *J. Chem. Phys.* **2009**, *130*, 074908.

(39) Prhashanna, A.; Khan, S. A.; Chen, S. B. Co-Micellization Behavior in Poloxamers: Dissipative Particle Dynamics Study. *J. Phys. Chem. B* **2015**, *119*, 572−582.

(40) Papadopoulou, V.; Kosmidis, K.; Vlachou, M.; Macheras, P. On the use of the Weibull function for the discernment of drug release mechanisms. *Int. J. Pharm.* **2006**, *309*, 44−50.

(41) Haase, M. F.; Brujic, J. Tailoring of High-Order Multiple Emulsions by the Liquid−Liquid Phase Separation of Ternary Mixtures. *Angew. Chem., Int. Ed.* **2014**, *53*, 11793−11797.

(42) Madan, P.; Microencapsulation, I. Phase separation or coacervation. *Drug Dev. Ind. Pharm.* **1978**, *4*, 95−116.

(43) Dobry, A.; Boyer-Kawenoki, F. Phase separation in polymer solution. *J. Polym. Sci.* **1947**, *2*, 90−100.

(44) Tian, Y.; Booth, J.; Meehan, E.; Jones, D. S.; Li, S.; Andrews, G. P. Construction of drug−polymer thermodynamic phase diagrams using Flory−Huggins interaction theory: identifying the relevance of temperature and drug weight fraction to phase separation within solid dispersions. *Mol. Pharmaceutics* **2013**, *10*, 236−248.